Combustion and Flame 276 (2025) 114136

Contents lists available at ScienceDirect

Combustion and Flame

journal homepage: www.sciencedirect.com/journal/combustion-and-flame

N-containing pollutant formation in pyrrole counterflow diffusion flames

Bingjie Chen [a,b], Sebastian Faller [b], Luna Pratali Maffei [c], Andrea Nobili [c,d], Matteo Pelucchi [c,*], Xingcai Lu [a], Heinz Pitsch [b]

[a] Key Laboratory for Power Machinery of M. O. E., Shanghai Jiao Tong University, Shanghai 200240, PR China
[b] Institute for Combustion Technology, RWTH Aachen University, Templergraben 64, Aachen 52056, Germany
[c] CRECK Modeling Lab, Department of Chemistry, Materials, and Chemical Engineering "Giulio Natta", Politecnico di Milano, Piazza Leonardo da Vinci 32, Milan 20133, Italy
[d] Department of Mechanical Engineering, Stanford University, Stanford 94305, CA, United States

ARTICLE INFO

Keywords:
Pyrrole
Kinetic model
N-containing pollutants
Counterflow flame
Biomass

ABSTRACT

Biomass conversion through direct combustion (energy production) or pyrolysis (bio-oil production) are novel concepts to reduce CO_2 emission in the energy sector. However, the nitrogen content in biomass feedstocks may result in elevated N-containing pollutants, e.g., NO_x, NH_3, HCN, and nitriles, yet their formation chemistry remains unclear. In this work, we studied N-containing pollutant formation in counterflow diffusion flames fuelled by pyrrole, a biomass tar surrogate component that accounts for the majority of fuel nitrogen. 27 species, including 8 N-containing species, were identified and measured in three flames with designed boundary conditions to reveal the influence of flame temperature and methane addition. Species mole fraction comparisons showed that methane addition and higher flame temperature promoted C_2–C_6 hydrocarbon formation, but mole fractions of N-containing species did not change much, reflecting less dependence on flame temperature or hydrocarbons in the species pool. An existing kinetic model for pyrrole pyrolysis and combustion was developed by updating the formation reactions of N-containing species based on recent literature studies. Numerical simulations using the kinetic model well reproduced mole fractions of most species except for NO and NO_2. Model analyses illustrated the nitrogen conversion pathways from pyrrole to individual N-containing pollutant species, and indicated the possible reactions for underestimated mole fractions of NO and NO_2. This work contributes to a better understanding of the combustion properties of N-containing fuels and N-containing pollutants in the context of biomass energy clean utilization.

1. Introduction

Biomass combustion is a promising solution to achieve carbon-neutrality and meet the increasing demand of energy supply [1]. However, the combustion process of protein-rich biomass or biomass-derived bio-oils with elevated nitrogen content may introduce N-containing pollutants from fuel nitrogen [2,3]. These N-containing pollutants, e.g., NO_x, NH_3, HCN, and nitriles are highly toxic and harmful to human health and environment [3,4]. Previous studies have reported emission levels of nitrogen oxides from biomass combustion ranging between 50 and 200 mg/MJ, as opposed to ~40 mg/MJ in the case of natural gas, highlighting a dominant role of fuel nitrogen [5]. Unravelling the N-containing pollutant formation chemistry is important to large-scale biomass energy clean utilization in advanced combustor design concepts [6].

As the simplest N-containing heterocyclic aromatic, pyrrole is widely used to represent the nitrogen content in coal, bio-oils, biomass waste, and biomass tar from devolatilization [7,8]. The molecular structures of coal [9] and biomass [7] have large amounts of pyrrolic and pyridinic functional groups to justify pyrrole and pyridine as representative N-containing surrogate components. The interesting molecular structures of pyrrole, nitrogen atom embedded in a five-membered heterocyclic aromatic ring, determines its reactivity and tendency to generate NO_x, HCN, and other N-containing pollutant species from fuel nitrogen in the pyrrolic functional groups in biomass [3,10].

Over the past half century, many studies have focused on exploring the pyrolysis [11–19] and combustion [10,20–31] chemistry of pyrrole. Based on experiments and theoretical calculations, kinetic models [14,16,23,26,30] were proposed to describe the pyrolysis/combustion chemistry of pyrrole, and to predict various experimental measurements

* Corresponding author.
E-mail address: matteo.pelucchi@polimi.it (M. Pelucchi).

https://doi.org/10.1016/j.combustflame.2025.114136
Received 9 December 2024; Received in revised form 20 March 2025; Accepted 22 March 2025
Available online 29 March 2025
0010-2180/© 2025 The Authors. Published by Elsevier Inc. on behalf of The Combustion Institute. This is an open access article under the CC BY-NC-ND license (http://creativecommons.org/licenses/by-nc-nd/4.0/).

like ignition delay time, flame speed, and speciation data in different reaction systems. Table 1 summarizes the previous experimental and kinetic modeling work on pyrrole pyrolysis/combustion chemistry.

Despite these experimental and kinetic modeling works, uncertainty on the combustion chemistry of pyrrole and N-containing pollutant formation still remains [29]. Also, all of the investigated reaction systems are premixed, so the important diffusion process in practical combustion systems is not considered. Finally, the influence of biomass volatile components (e.g., methane from biomass devolatilization [3]) on gas-phase combustion, or methane addition in the co-firing process is also neglected. Depending on the specific process and feedstock characteristics (e.g., higher heating value), replacement of the fossil fuel by up to 100 % of biomass have been reported, with ranges between 30–50 % as the most common cases [32,33].

Therefore, combustion chemistry and N-containing pollutant formation are investigated in this work in pyrrole counterflow diffusion flames. Besides a counterflow flame fuelled by pure pyrrole, two additional counterflow flames fuelled by pyrrole and methane were designed to reveal the influence of flame temperature and methane addition. The species measurements by time-of-flight molecular-beam mass-spectrometry (ToF-MBMS) showed that methane addition or higher flame temperature promoted the formation of C_2–C_6 hydrocarbons, but had only minor influence on N-containing pollutant species. Based on our previous work [29], a kinetic model is developed and updated to account for pyridine formation as reported in [34]. Numerical simulations using the developed kinetic model reproduce the measured mole fractions within experimental uncertainties for most species except NO and NO_2. The analyses indicated the possible reasons for such shortcomings by focusing on nitrogen conversion pathways from pyrrole to individual N-containing pollutant species. This work advances the understanding of N-containing fuel combustion and N-containing pollutant formation in the context of nitrogen-rich biomass like algae and sewage sludge [35].

Table 1
Experimental and kinetic modeling work on pyrolysis and combustion chemistry of pyrrole.

Experiments				
Reaction system	Reactor	Measurement target	Reference	Year
Pyrolysis	Flow reactor	Speciation	Axworthy et al. [11]	1978
	Shock tube	Speciation	Lifshitz et al. [12]	1989
	Shock tube	Speciation	Mackie et al. [14]	1991
	Flow reactor	Speciation	Hong et al. [13]	2009
	Jet-stirred reactor	Speciation	Wu et al. [19]	2022
Combustion/ Oxidation	Bunsen burner	Flame speed	Gibbs et al. [20]	1959
	Premixed flame	Speciation	Sloane et al. [21]	1980
	Flow reactor	Speciation	Lumbreras et al. [23]	2001
	Shock tube	Ignition delay	MacNamara et al. [31]	2003
	Flow reactor	Speciation	Koger et al. [10]	2005
	Premixed flame	Speciation	Tian et al. [22]	2007
	Flow reactor	Speciation	Yamamoto et al. [24]	2012
	Flow reactor	Speciation	Wang et al. [25]	2016
	Flow reactor	Speciation	Ren et al. [27]	2020
	Jet-stirred reactor	Speciation	Pelucchi et al. [26]	2021
	Shock tube	Ignition delay	Luo et al. [28]	2021
	Jet-stirred reactor	Speciation	Chen et al. [29]	2022
	Heat flux burner	Flame speed	Lubrano Lavadera et al. [30]	2022
Kinetic models				
Validation targets			References	Year
Speciation			Mackie et al. [14]	1991
Speciation			Martoprawiro et al. [16]	1999
Speciation			Lumbreras et al. [23]	2001
Ignition delay, speciation			Pelucchi et al. [26]	2021
Ignition delay, speciation			Chen et al. [29]	2022
Flame speed, ignition delay, speciation			Lubrano Lavadera et al. [30]	2022

2. Methodology

2.1. Counterflow burner configurations

Detailed descriptions of the atmospheric pressure counterflow burner setup have been reported in previous literature [36,37], so only key information is provided here. The opposed co-axial nozzles have an outer diameter of 20mm, and are 10mm apart. Nitrogen co-flow is used to shield the flame from external perturbation. A 1-D flat stagnation plane is ensured from flow field calculations and experimental validation in a previous study [36]. Different sampling positions along the flame centerline are enabled using a manual translation stage.

The liquid fuel in a pressurized tank is fed to the vaporizer through a liquid mass flow controller (Bronkhorst, mini CORI-FLOW™ ML120V21, accuracy for liquid: ± 0.2 % of the set flow rate). The vaporizer is heated to 150 °C, and the fuel vapor is diluted and carried by argon (or argon/methane mixture) to the fuel side nozzle of the counterflow burner. The transfer line is heated to 130 °C to prevent condensation and thermal degradation of pyrrole (boiling point 130 °C). Oxygen diluted with argon is introduced to the oxidizer side nozzle of the counterflow burner. All gas flows are regulated by mass flow controllers (Alicat or Natec).

2.2. Design of experiments for three counterflow flames

Three different counterflow diffusion flames are designed and investigated, and their boundary conditions are summarized in Table 2. The first flame is fuelled only by argon-diluted pyrrole (referred to as pure pyrrole flame), and the inlet mole fraction of pyrrole on the fuel side nozzle is 5 %. To study the influence of methane addition and flame temperature on pollutant formation, two additional counterflow flames were designed. The second flame, referred to as Z_{st} *const* flame, has 2.5 % methane in mole fraction in addition to 5 % pyrrole on the fuel nozzle. A higher amount of methane addition is not pursued because it results in sooty flames that may block the quartz sampling nozzle. The velocity of the Z_{st} *const* flame is calculated to achieve the same stagnation plane position as the pure pyrrole flame. The third flame, referred to as T_{eq} *const* flame, has the same inlet composition on the fuel side with Z_{st} *const* flame, but the mole fraction of oxygen on the oxidizer side is reduced to achieve the same equilibrium temperature as the pure pyrrole flame. Momentum balance between the fuel and oxidizer sides as well as other boundary conditions, e.g., inlet temperature on the fuel/oxidizer side and strain rate, are kept the same among the three flames. The designed boundary conditions are intended to isolate the effect of methane addition and flame temperature. Note that as the inlet mole fractions of pyrrole on the fuel side do not vary, the inlet nitrogen content remains equal in the three flames.

2.3. Time-of-flight molecular-beam mass-spectrometry

ToF-MBMS is used for species identification and quantification in terms of their different molecular weights. Since detailed descriptions of ToF-MBMS have been presented in the literature [36], only key

Table 2
Boundary conditions for the investigated pyrrole counterflow diffusion flames.

Flame	Fuel side			Oxidizer side			strain rate (s^{-1})
	velocity (cm/s)	T (K)	inlet mole fractions, x (-)	velocity (cm/s)	T (K)	inlet mole fractions, x (-)	
pure pyrrole	20.5	400	0.05 C_4H_5N, 0.95 Ar	17.5	313	0.30 O_2, 0.70 Ar	60
Z_{st} *const*	20.0	400	0.025 CH_4, 0.05 C_4H_5N, 0.925 Ar	17.5	313	0.30 O_2, 0.70 Ar	60
T_{eq} *const*	20.7	400	0.025 CH_4, 0.05 C_4H_5N, 0.925 Ar	17.5	313	0.25 O_2, 0.75 Ar	60

information is provided here. A molecular beam generated by three stages of vacuum extracts gas samples directly from the counterflow flame via a quartz sampling nozzle with an orifice diameter of 30μm. The small diameter of the orifice minimizes the influence of sampling nozzle intrusion along the centerline, as shown by optical measurements on the same setup in previous work [36]. The molecules in the sample gas are then ionized by the electrons from thermionic emission of a heated tungsten filament. The ionized molecules are accelerated by an electric field into the flight tube, so molecules with different molecular weights can be separated by their different flight times, and then registered by the mass spectrometer detector for quantification. The mass resolution (m/Δm) of ToF-MBMS is approximately 4000.

Four energies (12, 14, 17, 18eV) are used to achieve high signals with minimum fragmentation for individual species detection and quantification. 25 positions along the flame centerline are scanned in all three flames. The sampling position is determined by the photos taken from a Canon EOS 1200D camera with a spatial accuracy of 0.2mm [37,38]. An examplary photo of the pure pyrrole flame with a demonstration of sampling position determination (h, distance from fuel side nozzle) is presented in Fig. 1. Videos are also recorded continuously during the measurement to check the flame stability. Note that the first sampling position starts around 1.0mm due to the thickness of the fragile quartz nozzle. Photos in Fig. 2 provide a comparative visual view of the three investigated counterflow flames: pure pyrrole flame, Z_{st} *const* flame, and T_{eq} *const* flame.

The data processing principle and procedure was reported by Baroncelli et al. [36] with one slight modification in this work. Mole fractions of argon are first determined by numerical simulation using the developed kinetic model. Signals of other species are then calculated by comparison to those of argon or other reference species under the same energy. A python script is written to automatically process the data in this work, and the results are double-checked by manual data processing [37]. For reactants, the uncertainty is estimated to be 15 % by cold gas calibration. For species with known electron ionization cross sections in the database [39] or from calculations [40], the uncertainty of the measured mole fractions is estimated to be a factor of 2 - 3. Detailed uncertainty for each specie is provided in Table S1 in Supplementary Material-1 (SM-1).

2.4. Kinetic modeling

The kinetic model developed in this work is based on our previous mechanism [29]. Rate constants of some important reactions have been modified based on recent evidence and rate constant determinations from the literature. Yang et al. [41] performed VRC-TST calculations to determine rate constants of barrierless reactions within the C_2–CN subset. In particular, new rate coefficients were proposed for the reaction $CH_2CN + CH_3$, which was found to be of high importance in pyrrole pyrolysis and oxidation [26,29]. The authors highlighted over two orders of magnitude difference between the previous temperature-independent value by Sendt et al. [42] of 2×10^{13} cm^3/mol/s, which was adopted in our previous model, and the new high-pressure limit from their theoretical calculation ($k = 3.4 \times 10^{10} \times T^{0.06} \times \exp(1700/RT)$ cm^3/mol/s). The newly proposed value, however, appears to be excessively low in comparison to reasonable analogous recombination reactions such as $CH_3 + C_3H_3$, for which generally accepted high-pressure limit values are in the order of $2 - 4 \times 10^{12}$ cm^3/mol/s, or even higher [43]. The reason for this discrepancy might be Yang et al's. use of a DFT method (M06–2X) for the determination of the potential, while high-accuracy rate constants for recombination reactions, especially those involving resonance-stabilized compounds, may require the use of multireference methods (e.g., CASPT2) [44]. To preserve satisfactory model performances in comparison to the different datasets summarized in Table 1, we adopted a temperature- and pressure-independent value of 5×10^{12} cm^3/mol/s, thus lowering our previous adopted value by a factor of 4. Many uncertainties are still related to the key recombination reaction $CH_2CN + CH_3$ that has been only partly addressed with suitable theoretical methods (i.e., CASPT2 VRC-TST [45]). This reaction is significant both in modelling ignition phenomena as well as reproducing profiles of releveant intermediates such as CH_3CN and C_2H_5CN (Section 3.2.1). A recent work by Lubrano Lavadera et al. [30] reported laminar flame speed measurements for pyrrole/air mixtures (φ=0.6 – 1.3) at atmospheric pressure and $T_u = 338$ K. The authors proposed a kinetic model based on the previous work by Pelucchi et al. [26] with new values for a set of pyrrole-specific reactions. Table 3 reports the modified rate constants based on Lubrano Lavadera et al. [30]. A species nomenclature for the developed model in this work is provided in Section 1 of SM-1.

A recent work by Chen et al. [34] investigated the formation chemistry of another important N-containing component, pyridine (C_5H_5N) through a combined experimental and theoretical reaction pathway exploration approach. Pyrolysis experiments were carried out in an atmospheric pressure jet-stirred reactor between 1100 and 1200 K for pure acetylene and for acetylene/acetonitrile (CH_3CN) and acetylene/acrylonitrile (CH_2CHCN) mixtures. Such an approach revealed new pyridine formation pathways from C_2H_2 + CHCHCN, $C_2H_3CN + C_2H_3$,

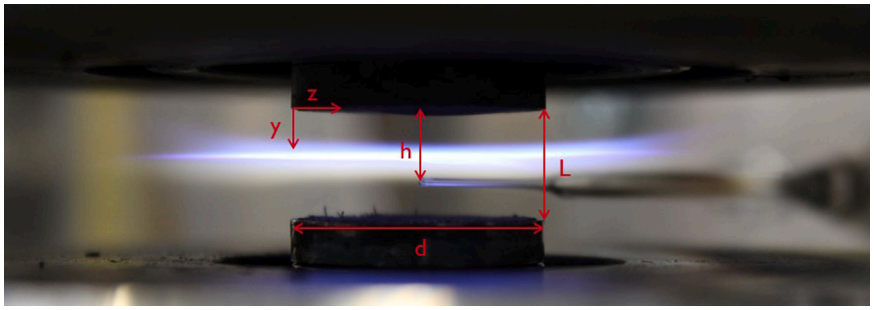

Fig. 1. Photo of pure pyrrole flame with demonstration of sampling nozzle position determination.

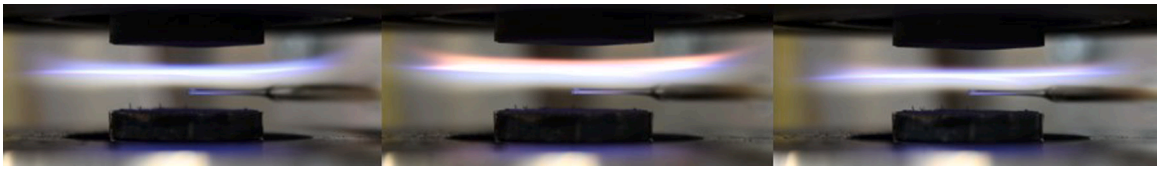

Fig. 2. Photos of pure pyrrole flame (left), Z_{st} *const flame* (middle), and T_{eq} const flame (right).

Table 3
Selected reactions revisited in the present model based on Lubrano Lavadera et al. [30]. Units are cm^3/mol/s, cal/mol. $k = A \times T^n \times \exp(-Ea/RT)$. Fuel specific species nomenclature and structures are provided at the bottom of the table complementary to complete list of Table S3.

Reaction	Rate constant			Reference and notes
	A (cm^3/mol/s)	n(-)	E_a (cal/mol)	
$OH + C_4H_5N \leftrightarrow H_2O + PYRLYL$	6.31×10^3	3.05	2540	[30]
duplicate	8.66×10^{31}	−6.38	3020	[30]
$O_2 + C_4H_5N \rightarrow HO_2 + PYRLYL$	8×10^{13}	0.00	37,150	[26]
$HO_2 + PYRLYL \rightarrow O_2 + C_4H_5N$	2×10^{13}	0.00	0	[30] $A \times 2$, irreversible
$A\text{-}C_3H_4CN + HO_2 \leftrightarrow OH + C_4H_4NO$	3.6×10^{23}	−2.5	15,000	[30] $A \times 2$
$C\text{-}C_3H_4CN + O_2 \leftrightarrow C_4H_4NO + O$	7.00×10^{20}	−2.5	15,000	[30]
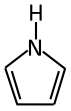		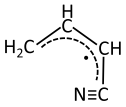	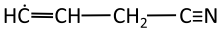	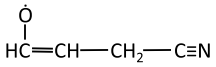
C_4H_5N	PYRLYL	A-C_3H_4CN	C-C_3H_4CN	C_4H_4NO

$CH_2CN + C_3H_3$, and $HCN + n\text{-}C_4H_5$. Formation of pyridine was found to be largely associated with $C_2H_2 + CHCHCN \rightarrow C_5H_4N$ followed by $H + C_5H_4N \rightarrow C_5H_5N$ in the acrylonitrile/acetylene reaction system. In the acetonitrile/acetylene case, the main contributor is $CH_2CN + C_3H_3 \rightarrow CH_2CCHCH_2CN$ where the latter linear cyanide structure undergoes cyclization to C_5H_5N. The new model of this work implements the above formation pathways from the work of Chen et al. [34] including the species thermodynamic properties. H-atom abstraction reactions for the generalized $R + C_5H_5N \leftrightarrow RH + C_5H_4N$ reaction are evaluated based on the systematic approach of Ranzi et al. [46] by assuming specific site corrections for the five vinyl type on the pyridine ring. The decomposition of C_5H_4N is described as in Chen et al. [29]. The acrylonitrile reaction with vinyl radical leads to the formation of $CH_2CHCHCHCN$ (2, 4-pentadienenitrile) according to the reaction $CH_2CHCN + C_2H_3 \rightarrow CH_2CHCHCHCN + H$ proposed by Chen et al. [29]. H-atom abstraction reactions consuming 2,5-pentadienenitrile were also included based on analogies with rate constants adopted for CH_2CHCN in our previous model, directly leading to the decomposition products according to irreversible lumped abstraction/decomposition reactions $R + CH_2CHCHCHCN \rightarrow RH + C_2H_2 + C_2H_2 + CN$.

Aiming for a general validated model, validation targets beyond the new counterflow flame data in the literature were considered. A full comparison with the existing targets is reported in Section 2 of SM-1. Specifically, ignition delay time [31], pyrolysis/combustion speciation in jet stirred reactor [19,26,29], flow reactor [23,24], shock tube [14], and laminar burning velocity [30] reported in previous literature were validated. The developed kinetic model well predicts most of the validation targets, except for laminar burning velocity. Introducing the modifications suggested from Lubrano Lavadera et al. [30] discussed above leads to slightly improved laminar flame speed predictions, as discussed in Section 2 of SM-1. However, experimental laminar flame speeds are still overpredicted by 18% at the peak value (Figure S9). This is largely due to the higher rate constant for the H-abstraction reaction $OH + C_4H_5N \leftrightarrow H_2O + PYRLYL$. Based on the sensitivity analysis of Figure S10, remaining deviations may be addressed by increasing the rate constant for H-abstraction reaction $H + C_4H_5N \leftrightarrow H_2 + PYRLYL$, showing a negative sensitivity coefficient to laminar burning velocity predictions. However, from extensive model testing, modifications in this direction caused worse predictions of JSR speciation data under pyrolysis and oxidation conditions [26,29], as well as for ignition delay times [31]. Moreover, the rate constant for $H + C_4H_5N \leftrightarrow H_2 + PYRLYL$ was theoretically determined in our previous work [29], thus a lower uncertainty compared to other key reactions in the kinetic model is expected (i.e., factor of ~2). For the above reasons, additional tuning towards improved laminar burning velocities predictions was not implemented in the current model to preserve good agreement with the remaining targets. Some discussions are included in Section 2 in SM-1. Based on sensitivity analyses, to improve agreement with new and already available experimental targets from previous works, we introduced some additional modifications as summarized in Table 4. It should be noted that the current version of the model (i.e., Chen et al. [29] and this work) considers two possible radical intermediates in pyrrole pyrolysis and oxidation: the resonance stabilized pyrlyl radical (PYRLYL) and one lumped vinyl type radical (C_4H_4N) representative of both the vinyl functions available in α and β sites to the nitrogen atom, which was not considered by neither Lubrano Lavadera et al. [30] nor the initial model of Pelucchi et al. [26]. The kinetic model files (kinetics, thermodynamics, transport) are provided in SM-2.

3. Results and discussions

27 species, including 8 N-containing pollutant species, were identified and quantified by ToF-MBMS measurements in the three investigated counterflow flames. Species mole fraction profiles are presented in Figs. 3, 4, 7, 9, 11 for comparison among the three flames. Black squares are measured data for the pure pyrrole flame; blue circles for the Z_{st} *const* flame; red triangles for the T_{eq} *const* flame. Lines with different colors represent simulated species mole fractions, and shaded areas indicate experimental uncertainty in the respective flames. SM-3 provides all experimental data of the three flames. Simulations of the counterflow flame were carried out using the OpenSMOKE++ by Cuoci et al. [47] with the 1-D laminar flame solver. To ensure the smoothness of calculated profiles, gradient and curvature coefficients of the solutions are set to 0.05 and 0.5, respectively, which lead to a total number of grid points of ~ 300 upon convergence.

Table 4
Modified reaction rate constants compared to our previous work [29]. Units are cm^3/mol/s and cal/mol. $k = A \times T^n \times \exp(-Ea/RT)$. Fuel specific species nomenclature and structures are provided at the bottom of the table complementary to complete list of Table S3.

Reaction	Rate constant			Reference and notes
	A (cm^3/mol/s)	n (-)	Ea (cal/mol)	
PYRLNE ↔ $H + A\text{-}C_3H_4CN$	3.06×10^{17}	0.00	86,746	[29] $A \times 1.5$
$O_2 + A\text{-}C_3H_5CN \leftrightarrow HO_2 + A\text{-}C_3H_4CN$	2.50×10^{13}	0.00	37,190	[29] A/2
$O_2 + C_4H_5N \rightarrow HO_2 + C_4H_4N$	1.87×10^{7}	2.00	54,834	[29] irreversible
$HO_2 + PYRLYL \rightarrow O_2 + C_4H_4N$	1.00×10^{13}	0.00	0	[29] irreversible
$A\text{-}C_3H_4CN + HO_2 \leftrightarrow A\text{-}C_3H_4CNOOH$	2.00×10^{44}	−10.6	7851	[29] A/3
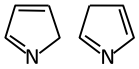	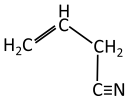	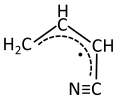	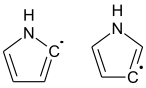	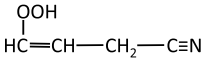
PYRLNE	AC_3H_5CN	A-C_3H_4CN	C_4H_4N	A-C_3H_4CNOOH

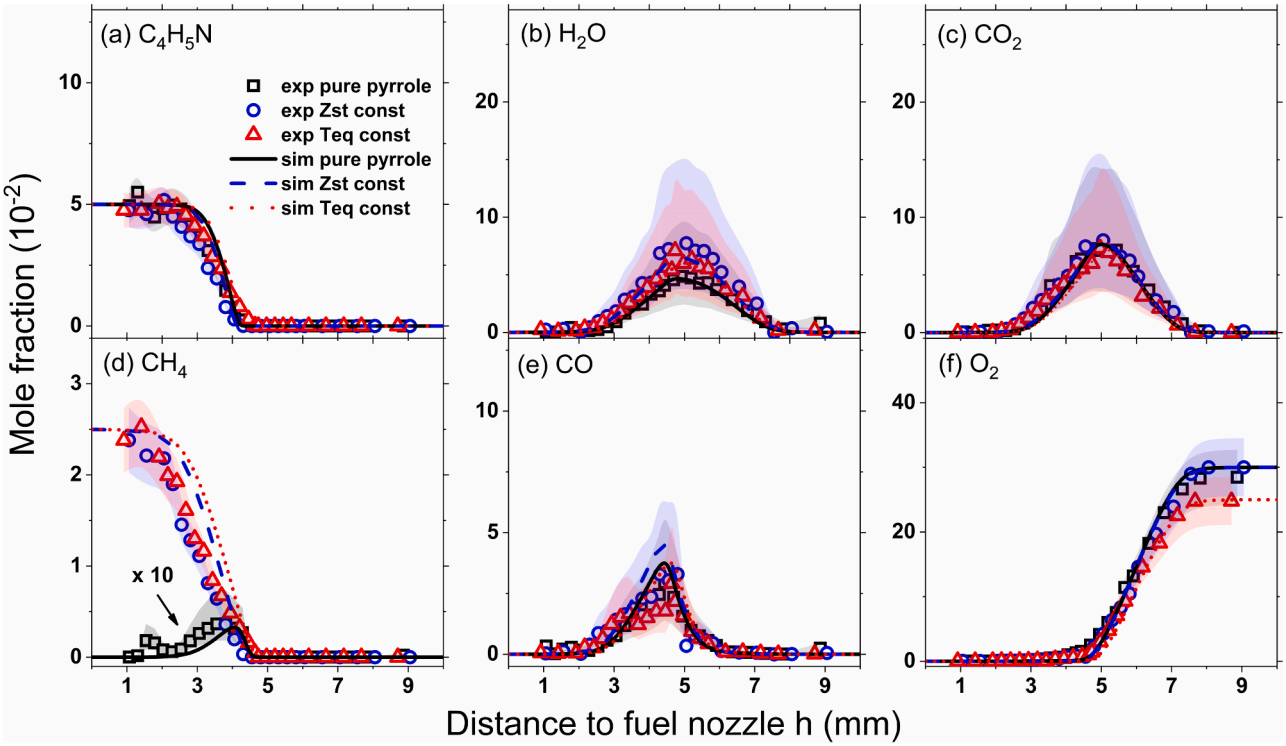

Fig. 3. Mole fraction profiles of reactants and main products in three counterflow flames (pure pyrrole flame, *Z_{st} const flame*, and T_{eq} const flame).

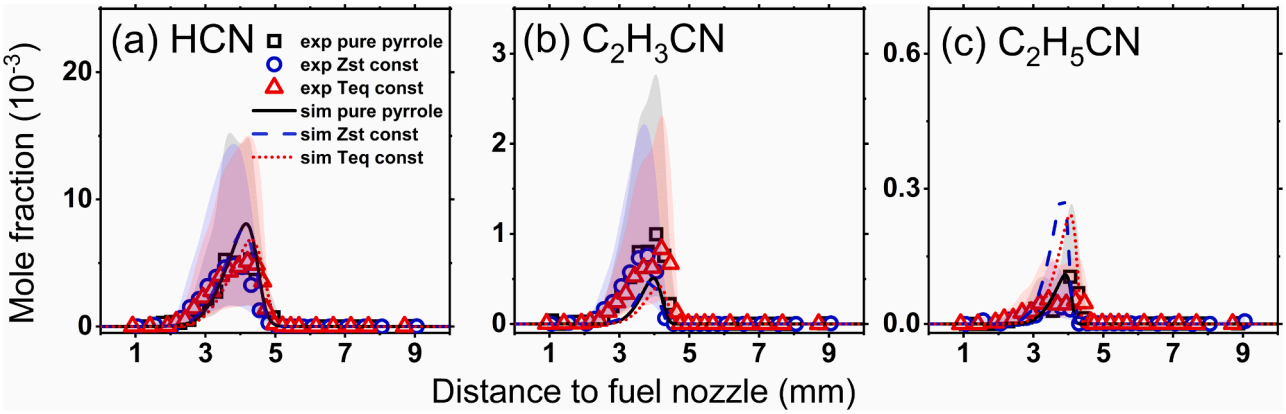

Fig. 4. Mole fraction profiles of three nitriles in three counterflow flames (pure pyrrole flame, *Z_{st} const flame*, and T_{eq} const flame).

3.1. Reactants and main products

Mole fractions of reactants (C_4H_5N, CH_4, O_2) and main products (H_2O, CO, CO_2) are presented in Fig. 3. In all three flames, both pyrrole and CH_4 are fully consumed around h (distance to fuel side nozzle) = 4mm, a borderline between the pyrolysis-dominated and the flame region. Among the three flames, the mole fractions of pyrrole and CO_2 do not change much, while the mole fractions of H_2O increase in the Z_{st} *const* and T_{eq} *const* flames. Methane addition in Z_{st} *const* and T_{eq} *const* flames may account for the increased H_2O mole fractions with more hydrogen content. For CO, its mole fractions are increased only in the Z_{st} *const* flame. This might be explained by the higher flame temperatures in the Z_{st} *const* flame, resulting in the shift of the chemical equilibrium of reaction $2CO + O_2 \leftrightarrow 2CO_2$. Numerical simulations using the developed kinetic model well reproduce the measured mole fractions of reactants and main products among the three flames. This indicates that the developed kinetic model can well describe the fuel consumption and reaction zone of the three target counterflow flames, and serve as the basis for investigating the formation chemistry of N-containing pollutant species in the following sections.

3.2. pollutants

The detected and measured N-containing species can be classified as: (1) nitriles, including hydrogen cyanide (HCN), acrylnitrile (C_2H_3CN), and propionitrile (C_2H_5CN). Acetonitrile (CH_3CN) is not reported because over 99 % of the signal comes from the fragmentation of pyrrole even at an energy of 12eV, while lower energies lead to overall low signal; (2) inorganic N-containig species, including nitrogen monoxide (NO), nitrogen dioxide (NO_2), and ammonia (NH_3); (3) Other N-containing species, including pyridine (C_5H_5N) and formamide (CH_3NO). Among these N-containing species, HCN and NO are the two most important species due to their high mole fractions, and they are also the major N-containing pollutants from fuel nitrogen in solid fuels [3,7].

3.2.1. Nitriles (HCN, C_2H_3CN, and C_2H_5CN)

Nitriles are an important pollutant species class originated from pyrrolic functional groups. The measured mole fractions of HCN, C_2H_3CN, and C_2H_5CN are shown in Fig. 4. From the measurement comparison among the three flame, the mole fractions of HCN, C_2H_3CN, and C_2H_5CN do not show significant change, indicating their independency to flame temperature or methane addition. Numerical simulations well predict the measured mole fractions within the experimental uncertainty. Both experiments and simulations indicate the maximum mole fractions of the three nitriles are around h = 4mm, where pyrrole and methane are fully consumed. This can be expected since most nitriles are produced from pyrolysis of pyrrole or pyridyl radical with ring-opening as initiation reactions. The model reproduces the experimental measurements within uncertainty, slightly underestimating the formation of acrylonitrile and slightly overestimating that of propionitrile.

Fig. 5 shows the representative results of a rate of production analysis to highlight the formation pathways of HCN. The analysis was carried out at h = 4 mm, and the fluxes are quite similar among the three flames. Five pathways produce HCN from pyrrole decomposition intermediates. The first one is from pyrrole molecular isomerization to allenic imine (HNCPROP), which was already highlighted as a relevant decomposition product in pyrrole pyrolysis [26]. The second source is hydrogen isocyanide (HNC) producing its isomer HCN through an isomerization reaction. HNC is mostly formed by H-atom abstraction reactions on both α and β sites of pyrrole to form the representative radical C_4H_4N. When the unpaired electron is located at the α position, a ring-opening reaction forms the linear isomer (LC_4H_4N) that rapidly decomposes to acetylene and HNC. The third source originates from the resonance-stabilized pyrlyl radical (PYRLYL) formed by H-atom

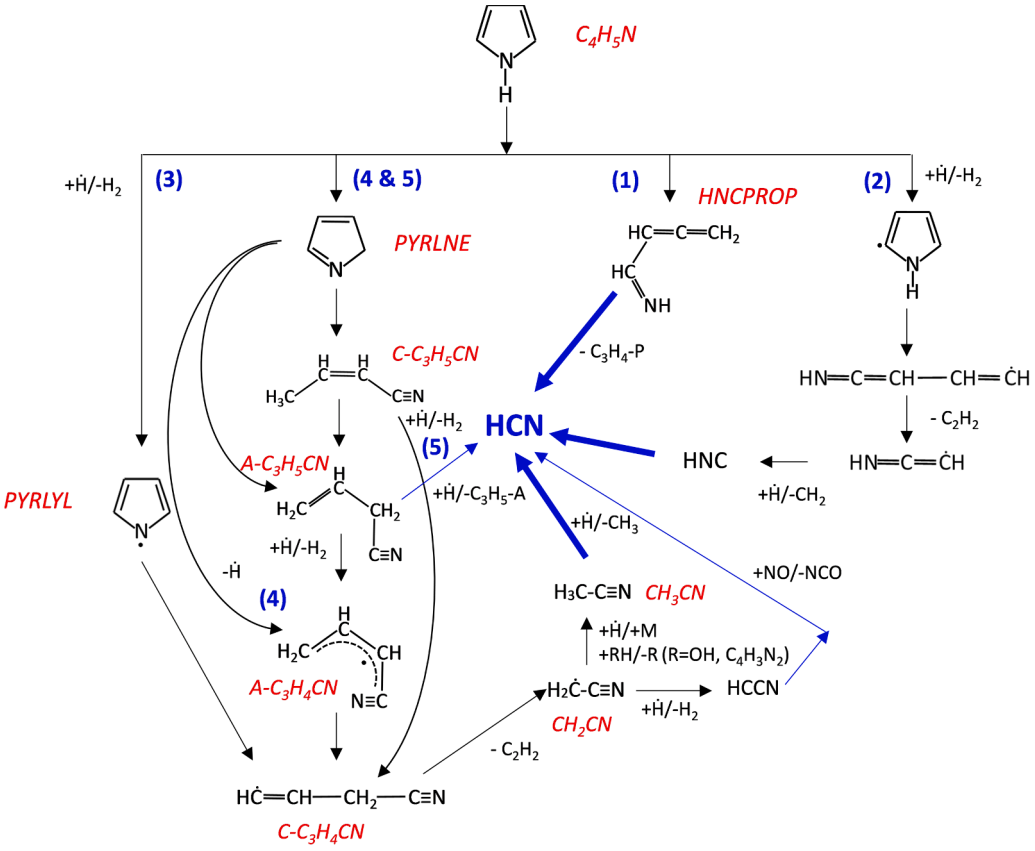

Fig. 5. Formation pathways (1 to 5) of HCN at h = 4mm in three pyrrole counterflow diffusion flames. Species names as in the model are reported in red.

abstractions with subsequent formation of cyano-propen-4-yl radical (C—C_3H_4CN). Further decomposition of C—C_3H_4CN produces the resonance-stabilized cyano methyl radical (CH_2CN) that can stabilize to CH_3CN by abstracting an H-atom or by H-atom recombination. The fourth source comes from the molecular isomerization of pyrrole to pyrrolenine (PYRLNE) through a series of unimolecular isomerization reactions and H-atom abstractions to C—C_3H_4CN. CH_3CN ultimately produces HCN by the addition of H and elimination of CH_3. Alternatively, CH_2CN can undergo H-atom abstraction to form HCCN (cyanomethylene radical), which subsequently reacts with NO to produce NCO and HCN according to a well-established de-NO_x reaction (HCCN + NO ↔ NCO + HCN). The last additional HCN formation pathway arises from the ring opening of pyrrolenine to allyl cyanide (A-C_3H_5CN) that undergoes H addition-elimination reaction with allyl radical as a co-product.

A similar reaction subset is responsible for acrylonitrile (C_2H_3CN) and propionitrile (C_2H_5CN) formation as reported in Fig. 6. Here, CH_2CN plays a significant role, in particular by its recombination reactions. Self-recombination leads to the formation of butanedinitrile ($C_4H_4N_2$). Its radical ($C_4H_3N_2$) produced from H-atom abstraction reactions decomposes through a beta-scission reaction to form cyanide (CN) and acrylonitrile. The addition of H to butanedinitrile leads to HCN elimination, forming the primary radical of propionitrile (CH_2CH_2CN) that dehydrogenates to C_2H_3CN through beta-scission. Recombination of CH_2CN with CH_3 directly forms C_2H_5CN that can undergo H-atom abstraction to form its primary or secondary radicals, and both radicals dehydrogenate to C_2H_3CN. As indicated by the percentage contribution to C_2H_3CN formation, methane addition promotes recombination of CH_2CN and CH_3 over self-recombination due to a higher amount of methyl radicals. A minor contribution to C_2H_3CN formation may also come from H addition to C—C_3H_5CN followed by the elimination of CH_3. Referring back to Fig. 4, it is clear from this analysis that refinement of rate constants for H-atom abstraction reactions on propionitrile beyond current analogy rules may drive further improvements by decreasing C_2H_5CN concentrations and thereby increasing C_2H_3CN yields.

3.2.2. *Inorganic N-containig species (NO, NO_2, and NH_3)*

NO, NO_2, and NH_3 are another important class of N-containing pollutants. Their mole fractions by experiments and kinetic modeling are compared in Fig. 7. The model predicts accurately the yields of ammonia, but strongly underestimates NO and NO_2 formation. These discrepancies should be addressed from both experimental and kinetic modelling aspects in future work. Experimentally, NO_x measurements by FTIR could be more accurate (~20%), less than the uncertainty of NO_x measurements by ToF-MS is a factor of 2 in this work. However, even considering the uncertainty, the models in both the previous work and this work (see Fig. S11 in SM-1) still underpredict NO_x. As the main source of NO_x, i.e., HCN, is well predicted in Fig. 4, additional investigations are required to revisit the conversion from HCN to NO_x.

Ammonia is produced by H-atom abstractions of NH_2 radical from H_2 and H_2O. Unlike similar HCN mole fraction profiles among the three investigated flames, two peaks can be observed for ammonia when methane is present in the Z_{st} *const* and the T_{eq} *const* flames. The additional methane undergoes H-atom abstraction by NH_2 forming methyl and ammonia. NH_2 is produced by the reaction $H + HNCO \leftrightarrow NH_2 + CO$, where HNCO directly derives from HCN upon isomerization to HNC and the addition of OH followed by H elimination, resulting in the first peak on mole fraction profiles of ammonia. The second peak was not captured, which requires further model investigations.

Successive H-atom abstraction reactions on NH_2 lead to the formation of NH as the major intermediate towards NO formation according to three main pathways, as shown in the rate of production analysis at h = 5 mm reported in Fig. 8a. NH is converted to HNO by addition of OH followed by H elimination. H-atom abstractions on HNO successively form NO H-atom abstractions on NH form N, which is converted to NO through typical thermal NO_x pathways ($N + O_2 \leftrightarrow NO + O$, $N + OH \leftrightarrow NO + H$). A direct conversion of NH to NO also occurs through the reaction $NH + O \leftrightarrow NO + H$. NO can be oxidized to NO_2 through $NO + O + M \leftrightarrow NO_2 + M$, or reduced to N_2 through $NO + N \leftrightarrow N_2 + O$. Addition of NH followed by H elimination is responsible for N_2O formation. While the experimental detection of the latter is challenging due to possible overlapping signal with CO_2, model simulations predict peak concentrations in the order of 100 ppm.

Results from a sensitivity analysis to NO formation at h = 5 mm in Fig. 8b confirm the coexistence of both thermal and prompt NO_x formation pathways arising from HCN, therefore directly triggered by the N element in biomass feedstock. The reburning (or deNO_x) mechanism converting N to N_2 is the major reason for NO reduction. No significant differences are highlighted in terms of sensitivity coefficients to the most sensitive reactions in the three investigated flames. Based on the

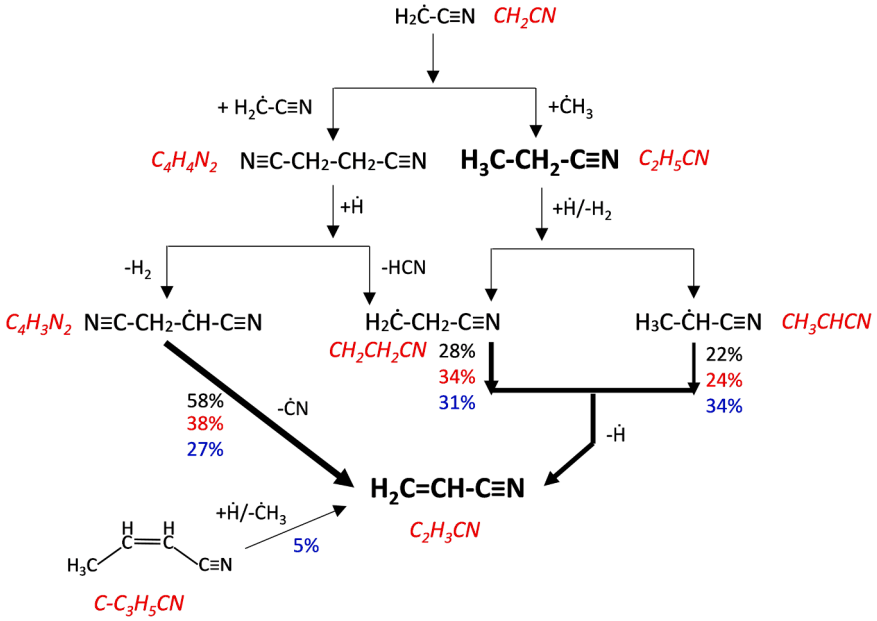

Fig. 6. Formation pathways of C_2H_3CN and C_2H_5CN at h = 4mm in pure pyrrole flame, Z_{st} *const flame*, and T_{eq} const flame. Numbers indicate relative importance towards formation of C_2H_3CN. Species names as in the model are reported in red.

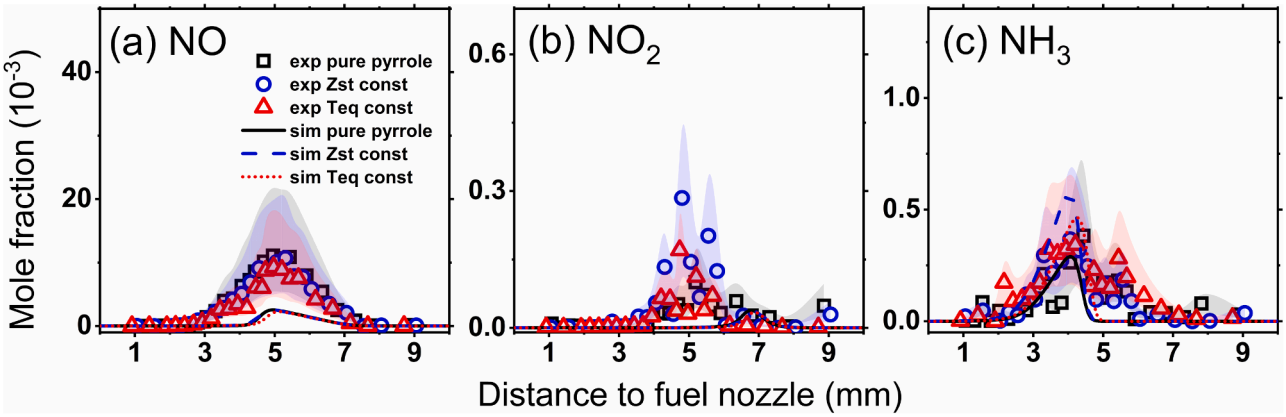

Fig. 7. Mole fraction profiles of NO, NO_2, and NH_3 in three counterflow flames (pure pyrrole flame, *Z_{st} const flame*, and T_{eq} const flame).

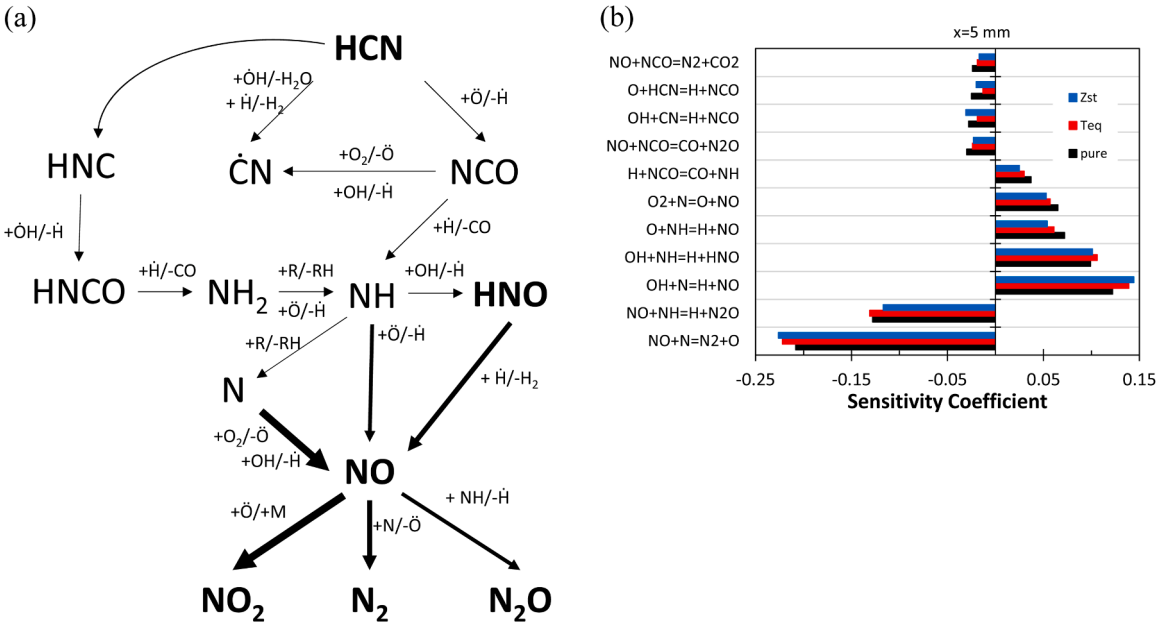

Fig. 8. Rate of production (a) and sensitivity (b) analyses of NO formation/consumption.

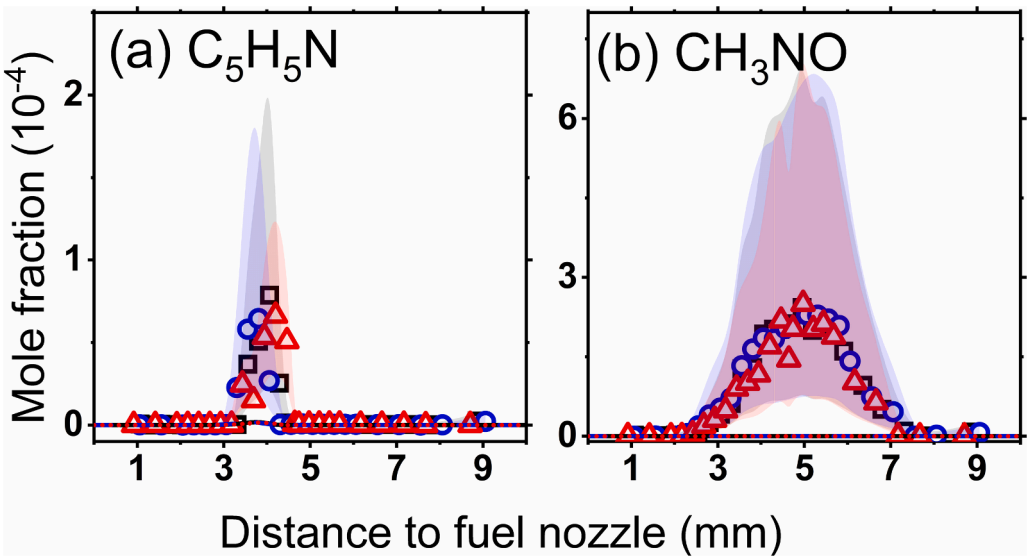

Fig. 9. Mole fraction profiles of pyridine and CH_3NO in three counterflow flames (pure pyrrole flame, *Z_{st} const flame*, and T_{eq} const flame).

analyses and agreement between model and experiments concerning HCN prediction, it is hard to foresee significant margins to improve NO and NO_2 predictions. It should be noted that the underlying NO_x formation/consumption subset has been extensively validated [48], and ad hoc tuning for the specific pyrrole case is outside the scope of this study.

3.2.3. Pyridine (C_5H_5N)

As discussed in Section 2, a recent work by Chen et al. [34] focused on the formation of pyridine during the pyrolysis of acetonitrile/acrylonitrile with acetylene. The reported major pyridine formation pathways with potential energy surfaces and preliminary rate constants were implemented in the present model, and predictions of pyridine formation are compared with experimental measurements in Fig. 9. Once again, no significant differences are observed among the three flame configurations. Mole fractions of the C_5H_5N peak at $h = 4$ mm where pyrrole is mostly consumed, which means decomposition of pyrrole happen first, and the small molecule products recombine to produce pyridine. The model strongly underestimates pyridine formation, despite accurately capturing the peak location. Pyridine formation is triggered by the recombination of two resonance-stabilized radicals, namely the propargyl radical (C_3H_3) and the cyano methyl radical (CH_2CN). The formed cyanide intermediate CH_2CCHCH_2CN can undergo cyclization to pyridine. Pyridine is then consumed by H-atom abstractions to yield pyridine radical (C_5H_4N) that decomposes through a ring-opening beta-scission to acetylene and acrylonitrile radical (CHCHCN). CHCHCN further decomposes to acetylene and CN. Alternatively, pyridine can undergo H addition followed by HCN elimination to form C_4H_5 (1-butyn-3yl radical), which further dehydrogenates to vinylacetylene (C_4H_4).

Results from a sensitivity analysis to C_5H_5N formation are reported in Fig. 10. In general, consumption pathways of CH_2CN alternative to the major pyridine formation channel highlighted above have a negative sensitivity coefficient as they compete directly with pyridine formation. In particular, the self-recombination of CH_2CN and H-atom abstraction by CH_2CN have a negative sensitivity coefficient. The same rationale applies to reactions consuming propargyl radical. On the contrary, reactions directly or indirectly forming C_3H_3 (e.g., H-atom abstractions from propyne, and molecular decomposition of pyrrole to HNCPROP, see Fig. 5) promote pyridine formation.

Formamide (CH_3NO) is also measured in the targeted flames with no impact of methane addition. The kinetic model only predicts trace amounts of CH_3NO ($\sim 10^{-8}$) compared to the experimental data ($\sim 10^{-4}$). CH_3NO is mostly formed by the direct interaction of methyl radical with NO in the kinetic model. The lack of sensitivity to the presence of methane at the fuel side suggests potential missing reactions to produce CH_3NO as well as possible experimental uncertainties derived for instance from the wide electron energy distribution and uncertainties in the electron-impact ionization cross-section. Measurements by FTIR or other diagnostic methods may provide more accurate measurements, as well as theoretically exploring missing CH_3NO formation reactions in future work.

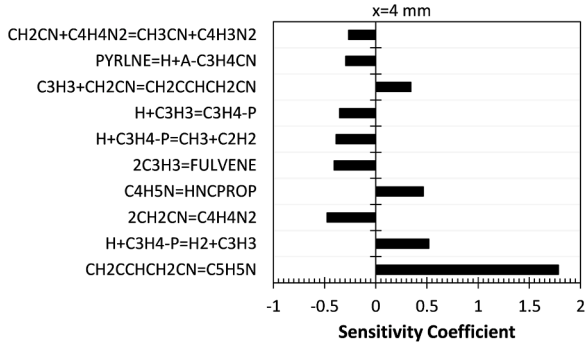

Fig. 10. Sensitivity analysis to C_5H_5N formation/consumption at $h = 4$ mm.

3.3. C_2–C_6 hydrocarbons

Contrary to the N-containing species, mole fractions of C_2–C_6 hydrocarbons are sensitive to methane addition or flame temperature. Fig. 11 shows the mole fraction profiles of nine C_2–C_6 hydrocarbons, e.g., acetylene (C_2H_2, Fig. 11a), ethylene (C_2H_4, Fig. 11b), hydrogen (H_2, Fig. 11c), allene + propyne (C_3H_4, Fig. 11d), propene (C_3H_6, Fig. 11e), 1,3-butadiene (C_4H_6, Fig. 11f), diacetylene (C_4H_2, Fig. 11 g), vinylacetylene (C_4H_4, Fig. 11h), and benzene (C_6H_6, Fig. 11i). Allene and propyne cannot be separated by electron ionization ToF-MBMS due to their close ionization energies (allene: 9.65eV [49], propyne: 10.25eV [50]) and wide energy distribution (~1eV) of the electrons emitted from the heated tungsten filament, so the sums of their mole fraction profiles from measurements and simulations are presented instead. These hydrocarbon molecules and radicals are important precursors for polycyclic aromatic hydrocarbons (PAHs) and soot [51]. It should be noted that, due to the wide energy distribution of electrons emitted from the tungsten filament, we cannot prevent the fragmentation of pyrrole. One of the pyrrole fragments is C_3H_6, hence its signal may come from pyrrole fragmentation. In our cold gas calibration (i.e., measurements without flames), C_3H_6 signal intensity deriving from fragmentation is very high, which constitutes the largest part of the signal measured in the actual flame. As a result, the flame signal corrected by reducing fragmentation part obtained in the gas calibration retains even a larger uncertainty.

From the comparison among the three flames, methane addition and higher flame temperature increase the mole fractions of most C_2–C_6 hydrocarbons, especially significant increase C_3H_4, but not for 1,3-butadiene in Fig. 4f. This can be expected because of more carbon amount with methane addition, and higher flame temperatures may facilitate H-atom abstraction from methane to form CH_3 radicals, which may add to other hydrocarbons to form C_2–C_6 hydrocarbons [36]. The declined mole fractions of 1,3-butadiene with methane addition or higher flame temperature might be due to the increased flux of its consumption reactions, $H + C_4H_6 \leftrightarrow C_2H_4 + C_2H_3$ and $H + C_4H_6 \leftrightarrow C_4H_5 + H_2$. The kinetic model simulations well capture the mole fractions of most C_2–C_6 hydrocarbons, with large discrepancies observed for propene due to the large reduction of the contribution from fragmentation.

The increased formation of larger hydrocarbons in the Z_{st} *const* and the T_{eq} *const* flames may enhance soot formation. From photos of the three counterflow flames in Fig. 2, a reddish layer above the blue flame (soot formation area [52]) appeared in the Z_{st} *const* and the T_{eq} *const* flames. This suggests a transition from a non-sooting to a sooting flame, and the flame temperature has a more pronuouced effect to promote soot formation by supplying C_2–C_6 hydrocarbons in the species pool.

To summarize, the developed kinetic model can well capture most of the species mole fractions in targeted pyrrole counterflow diffusion flames, except for NO, NO_2, C_5H_5N, and CH_3NO, which requires further investigations on their formation chemistry and kinetic model development.

4. Conclusions

N-containing pollutant formation chemistry is investigated in this work for three counterflow diffusion flames fuelled by pyrrole. The boundary conditions of the three target flames were designed to isolate the effects of methane addition and flame temperature. By time of flight molecular beam mass spectrometer, 27 species, including 8 N-containing pollutant species were detected and measured. Based on experimental results, a kinetic model for pyrrole was developed by updating formation reactions of individual N-containing pollutant species. The model was used to describe the combustion chemistry of pyrrole and the formation chemistry of N-containing pollutant species.

The results from both experiements and numerical simulations using the developed kinetic model indicate that mole fractions of N-containing

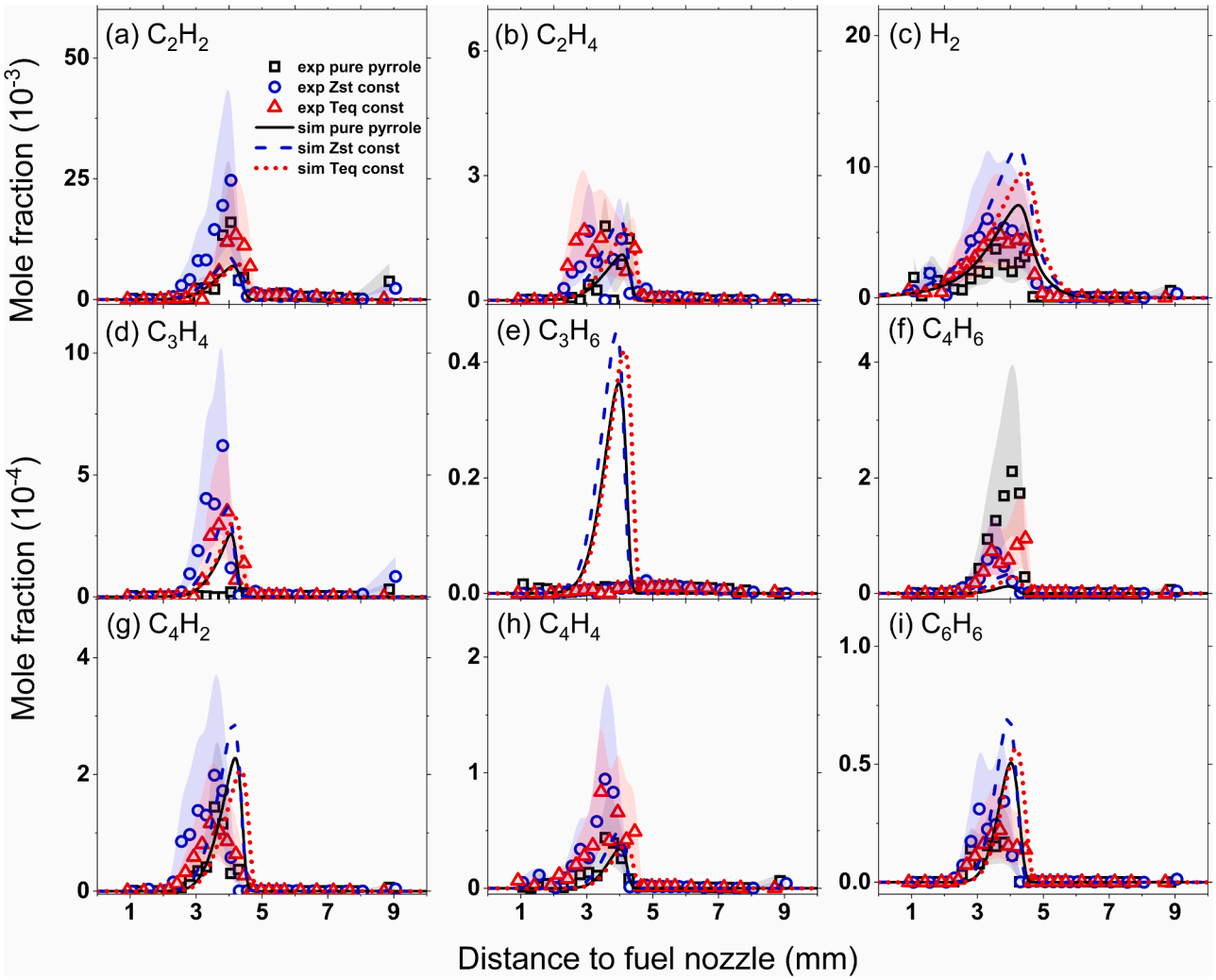

Fig. 11. Mole fraction profiles of hydrocarbon species in three counterflow flames (pure pyrrole flame, *Z_{st} const flame*, and T_{eq} const flame).

species do not change much among the three flames. In contrast, the formation of C_2–C_6 hydrocarbons is promoted with both higher flame temperature and methane addition. The formation of N-containing pollutant species depends less on methane addition or flame temperatures than the consumption of pyrrole and their formation reaction pathways. By updating the formation reactions, the developed kinetic model well described the formation pathways of most species by reproducing their measured mole fractions except for NO and NO_2. Further model development should focus on improving the predictions for NO_x. This work may help better understand how N-containing pollutant species are produced from fuel nitrogen of nitrogen-rich biomass in diffusion combustion.

5. Novelty and significance

Nitrogen-rich biomass is novel carbon neutral fuel, but its combustion process is a main source of N-containing pollutants. In this work, we investigated the formation chemistry of N-containing pollutant species, for the first time, in counterflow diffusion flames with designed boundary conditions fuelled by pyrrole as a biomass tar surrogate to represent fuel nitrogen in biomass. It was found that the formation of N-containing pollutant species is less dependent on flame temperature and species pool, but more on the combustion chemistry of pyrrole and the formation reactions of N-containing pollutants. The formation pathways of N-containing pollutants and influence of boundary conditions were unraveled by developed kinetic model while keeping good agreement with previously reported reaction characteristics in the literature. This work advances understanding of N-containing pollutant formation from fuel nitrogen in biomass, which can help to develop smart control strategy for advanced biomass combustion system.

CRediT authorship contribution statement

Bingjie Chen: Writing – review & editing, Writing – original draft, Validation, Methodology, Investigation, Formal analysis, Data curation, Conceptualization. **Sebastian Faller:** Investigation, Data curation. **Luna Pratali Maffei:** Writing – review & editing, Validation, Methodology, Investigation. **Andrea Nobili:** Writing – review & editing, Validation, Methodology, Investigation, Data curation, Conceptualization. **Matteo Pelucchi:** Writing – review & editing, Writing – original draft, Validation, Supervision, Methodology, Formal analysis, Conceptualization. **Xingcai Lu:** Writing – review & editing, Resources, Project administration, Investigation, Data curation, Conceptualization. **Heinz Pitsch:** Writing – review & editing, Writing – original draft, Supervision, Resources, Project administration, Methodology.

Declaration of competing interest

The authors declare that they have no known competing financial interests or personal relationships that could have appeared to influence the work reported in this paper.

Acknowledgements

The authors (SJTU) gratefully acknowledge the funding support from the National Natural Science Foundation of China (NO. W2411043) The authors from RWTH Aachen acknowledge the financial support by the Deutsche Forschungsgemeinschaft within the framework of the collaborative research center SFB/Transregio 129 “Oxyflame”. The kinetic modeling work at Politecnico di Milano was funded by the European Union’s Horizon 2020 Research and Innovation Program (Grant Agreement 723706 - IMPROOF Project, H2020-IND-CE-2016-17/H2020-SPIRE-S016) and (for LPM) by NEST - Network 4 Energy Sustainable Transition (D.D. 1561 11/10/2022, PE0000021).

Supplementary materials

Supplementary material associated with this article can be found, in the online version, at doi:10.1016/j.combustflame.2025.114136.

References

[1] S. Chu, A. Majumdar, Opportunities and challenges for a sustainable energy future, Nature 488 (7411) (2012) 294–303.
[2] P. Glarborg, et al., Modeling nitrogen chemistry in combustion, Prog. Energy Combust. Sci. 67 (C) (2018) 31–68.
[3] A. Williams, et al., Pollutants from the combustion of solid biomass fuels, Prog Energ Combust. 38 (2) (2012) 113–137.
[4] R. Zhang, et al., *Selective transformation of various nitrogen-containing exhaust gases toward* N_2*over zeolite catalysts*, Chem. Rev. 116 (6) (2016) 3658–3721.
[5] S. Ozgen, S. Cernuschi, S. Caserini, An overview of nitrogen oxides emissions from biomass combustion for domestic heat production, Renew. Sustain. Energy Rev. 135 (2021) 110113.
[6] M. Hupa, O. Karlström, E. Vainio, Biomass combustion technology development – it is all about chemical details, Proc. Combust. Inst. 36 (1) (2017) 113–134.
[7] P. Glarborg, A.D. Jensen, J.E. Johnsson, Fuel nitrogen conversion in solid fuel fired systems, Prog. Energ. Combust. 29 (2) (2003) 89–113.
[8] P.E.A. Debiagi, et al., Algae characterization and multistep pyrolysis mechanism, J. Anal. Appl. Pyrolysis. 128 (2017) 423–436.
[9] J.A. Miller, C.T. Bowman, Mechanism and modeling of nitrogen chemistry in combustion, Prog. Energy Combust. Sci. 15 (4) (1989) 287–338.
[10] S. Koger, H. Bockhorn, NO x formation from ammonia, hydrogen cyanide, pyrrole, and caprolactam under incinerator conditions, Proc. Combust. Inst. 30 (1) (2005) 1201–1209.
[11] A.E. Axworthy, V.H. Dayan, G.B. Martin, Reactions of fuel-nitrogen compounds under conditions of inert pyrolysis, Fuel (Guildford) 57 (1) (1978) 29–35.
[12] A. Lifshitz, C. Tamburu, A. Suslensky, Isomerization and decomposition of pyrrole at elevated temperatures: studies with a single-pulse shock tube, J. Phys. Chem. 93 (15) (1989) 5802–5808.
[13] X. Hong, et al., An experimental and theoretical study of pyrrole pyrolysis with tunable synchrotron VUV photoionization and molecular-beam mass spectrometry, J. Phys. Chem. A 113 (18) (2009) 5397–5405.
[14] J.C. Mackie, et al., Shock tube pyrolysis of pyrrole and kinetic modeling, Int. J. Chem. Kinet. 23 (8) (1991) 733–760.
[15] F. Dubnikova, A. Lifshitz, Isomerization of pyrrole. Quantum chemical calculations and kinetic modeling, J. Phys. Chem. A 102 (52) (1998) 10880–10888.
[16] M. Martoprawiro, G.B. Bacskay, J.C. Mackie, Ab initio Quantum chemical and kinetic modeling study of the pyrolysis kinetics of pyrrole, J. Phys. Chem. A 103 (20) (1999) 3923–3934.
[17] G.B. Bacskay, M. Martoprawiro, J.C. Mackie, The thermal decomposition of pyrrole: an ab initio quantum chemical study of the potential energy surface associated with the hydrogen cyanide plus propyne channel, Chem. Phys. Lett. 300 (3) (1999) 321–330.
[18] L. Zhai, X. Zhou, R. Liu, A theoretical study of pyrolysis mechanisms of pyrrole, J. Phys. Chem. A 103 (20) (1999) 3917–3922.
[19] L.-N. Wu, et al., Dinitriles and nitriles are common intermediates of pyrrole pyrolysis, Combust. Flame 245 (2022) 112358.
[20] G.J. Gibbs, H.F. Calcote, Effect of molecular structure on burning velocity, J. Chem. Eng. Data 4 (3) (1959) 226–237.
[21] T.M. Sloane, R.J. Brudzynski, J.W. Ratcliffe, Primary steps in the oxidation of pyridine and pyrrole added to a lean methane/oxygen/argon flame, Combust. Flame 38 (1980) 89–102.
[22] Z. Tian, et al., An experimental study of low-pressure premixed pyrrole/oxygen/argon flames with tunable synchrotron photoionization, Combust. Flame 151 (1) (2007) 347–365.
[23] M. Lumbreras, et al., A study of pyrrole oxidation under flow reactor conditions, Combust. Sci. Technol. 172 (1) (2001) 123–139.
[24] T. Yamamoto, et al., Kinetic study of fuel NO formation from pyrrole type nitrogen, Fuel 93 (1) (2012) 213–220.
[25] C. Wang, et al., *Pyridine and pyrrole oxidation under oxy-fuel conditions.* Energy sources, Part A, Recovery, Utiliz., Environ. Effects 38 (7) (2016) 975–981.
[26] M. Pelucchi, et al., Pyrolysis and combustion chemistry of pyrrole, a reference component for bio-oil surrogates: jet-stirred reactor experiments and kinetic modeling, Energy Fuels. 35 (9) (2021) 7265–7284.
[27] Q. Ren, et al., *Experimental study and mechanism analysis of NO formation during volatile-N model compounds combustion in* H_2O/CO_2atmosphere, Fuel (Guildford) 273 (2020) 117722.
[28] J. Luo, et al., *A shock tube and modeling study on the auto-ignition properties of pyrrole in* O_2/CO_2atmosphere *at elevated pressures*, Combust. Flame 230 (2021) 111458.
[29] B. Chen, et al., New insights into the oxidation chemistry of pyrrole, an N-containing biomass tar component, Proc. Combust. Inst. 39 (1) (2023) 73–84.
[30] M. Lubrano Lavadera, J. Chen, A.A. Konnov, Laminar burning velocities of pyrrole/air flames: experimental and comprehensive modeling study, Combust. Flame 245 (2022) 112350.
[31] J.P. MacNamara, J.M. Simmie, The high temperature oxidation of pyrrole and pyridine ignition delay times measured behind reflected shock waves, Combust. Flame 133 (3) (2003) 231–239.
[32] E. Agbor, et al., Integrated techno-economic and environmental assessments of sixty scenarios for co-firing biomass with coal and natural gas, Appl. Energy 169 (2016) 433–449.
[33] M.S. Roni, et al., Biomass co-firing technology with policies, challenges, and opportunities: a global review, Renew. Sustain. Energy Rev. 78 (C) (2017) 1089–1101.
[34] B. Chen, et al., On the formation of pyridine, the first nitrogen heterocyclic ring in NPAHs, Proc. Combust. Inst. 40 (1–4) (2024) 105675.
[35] J. Tao, et al., Biomass combustion: environmental impact of various precombustion processes, J. Clean. Prod. 261 (2020) 121217.
[36] M. Baroncelli, et al., Investigating the effect of oxy-fuel combustion and light coal volatiles interaction: a mass spectrometric study, Combust. Flame 204 (C) (2019) 320–330.
[37] B. Chen, et al., Exploring the combustion chemistry of anisole in laminar counterflow diffusion-flames under oxy-fuel conditions, Combust. Flame 243 (2022) 111929.
[38] M. Hellmuth, et al., Synergistic effect on PAH and soot formation in ethylene counterflow diffusion flames by the addition of 1,3-dioxolane - a bio-hybrid fuel, Proc. Combust. Inst. 39 (1) (2023) 899–908.
[39] Y. Kim, K.I., M.Rudd, M. Ali, P. Stone, J. Chang, J. Coursey, R. Dragoset, A. Kishore, K. Olsen. *Electron-impact ionization cross section for ionization and excitation database (version 3.0, 2004)*. 2008; Available from: http://www.nist.gov/pml/data/ionization/index.cfm.
[40] W.L. Fitch, A.D. Sauter, Calculation of relative electron impact total ionization cross sections for organic molecules, Anal. Chem. 55 (6) (1983) 832–835.
[41] Y. Yang, et al., Enhanced C2-CN sub-mechanism: impact on NO/N2O and soot precursor yields during C2H2/HCN oxidation, Combust. Flame 260 (2024) 113267.
[42] K. Sendt, et al., Ab initio Quantum chemical and experimental (Shock Tube) studies of the pyrolysis kinetics of acetonitrile, J. Phys. Chem. A 103 (8) (1999) 1054–1072.
[43] C. Huang, B. Yang, F. Zhang, Initiation mechanism of 1,3-butadiene combustion and its effect on soot precursors, Combust. Flame 184 (2017) 167–175.
[44] S.J. Klippenstein, L.B. Harding, A summary of “A direct transition State theory based study of Methyl Radical recombination kinetics, J. Phys. Chem. A 104 (11) (2000) 2351–2354.
[45] S.J. Klippenstein, From theoretical reaction dynamics to chemical modeling of combustion, Proc. Combust. Inst. 36 (1) (2017) 77–111.
[46] E. Ranzi, et al., Prediction of kinetic parameters for hydrogen abstraction reactions, Combust. Sci. Technol. 95 (1–6) (1994) 1–50.
[47] A. Cuoci, et al., OpenSMOKE++: an object-oriented framework for the numerical modeling of reactive systems with detailed kinetic mechanisms, Comput. Phys. Commun. 192 (2015) 237–264.
[48] Y. Song, et al., The sensitizing effects of NO2 and NO on methane low temperature oxidation in a jet stirred reactor, Proc. Combust. Inst. 37 (1) (2019) 667–675.
[49] B. Yang, et al., Absolute photoionization cross-sections of some combustion intermediates, Int. J. Mass Spectrom. 309 (2012) 118–128.
[50] T.A. Cool, et al., Photoionization cross sections for reaction intermediates in hydrocarbon combustion, Int. J. Mass Spectrom. 247 (1) (2005) 18–27.
[51] H. Wang, Formation of nascent soot and other condensed-phase materials in flames, P Combust Inst 33 (1) (2011) 41–67.
[52] Y. Wang, S.H. Chung, Soot formation in laminar counterflow flames, Prog. Energy Combust. Sci. 74 (2019) 152–238.